PROCEEDINGS, 50th Workshop on Geothermal Reservoir Engineering
Stanford University, Stanford, California, February 10-12, 2025
SGP-TR-229

Repurposing Oil/Gas Wells for Geothermal Applications: An Experimental Study on the Geothermal Impacts of the Cycling System

Wei Xiong[1,2]*; Thomas Paronish[3,4]; Meghan Brandi[1,2]; Justin Mackey[1,2]; Barbara Kutchko[1]; Dustin Crandall[3]; Danylo Oryshchyn[5]; Saeed Salehi[6]

[1]National Energy Technology Laboratory, 626 Cochran Mill Road, Pittsburgh, PA 15236, USA

[2]NETL Support Contractor, 626 Cochran Mill Road, Pittsburgh, PA 15236, USA

[3]National Energy Technology Laboratory, 3610 Collins Ferry Road, Morgantown, WV 26505, USA

[4]NETL Support Contractor, 3610 Collins Ferry Road, Morgantown, WV 26505, USA

[5]National Energy Technology Laboratory, 1450 SW Queen Avenue, Albany, OR 973213, USA

[6]Southern Methodist University, 6425 Boaz Lane, Dallas, TX 75275, USA

*Corresponding author: wei.xiong@netl.doe.gov

Keywords: Geothermal; Geochemistry; Corrosion; Rock-fluid interactions; Repurposing oil/gas wells

ABSTRACT

Repurposing late-stage, depleted, and/or inactive hydrocarbon wells for geothermal energy production can be environmentally sustainable and economically profitable. Studies of such transition systems tend to focus on geothermal properties, geomechanics, and the economic benefits of using simulation analysis. Laboratory research is needed to assess the geochemical impact of wells not originally drilled for geothermal purposes. Reservoir fluids may contain various dissolved salts and aqueous silica depending on the geologic formation type. Oil and gas reservoir fluids may also contain trace residual hydraulic fracturing chemicals and high total dissolved solids. The fluid-material interactions during the cycling of geothermal fluids may enhance pipe corrosion and scale mineral formation (silica, salts, etc.). It is crucial to studying the complicated fluids reactions with site-specific reservoir geochemistry in a geothermal system under repeated heating and cooling of fluids to understand the impacts to long-term performance.

Solid-fluid chemical interactions may introduce new scale species such as iron (hydro)oxides to the reservoir, resulting in changes to the fluid chemistry and causing subsequent reactions as the fluid is cycled through the entire geothermal system. In this study, we designed an experimental system mimicking the fluid paths cycling through fractured or porous reservoir at elevated temperature and pressure, and through the geothermal infrastructure materials (e.g., steel) at reduced temperature and pressures. We focused on answering fundamental geochemical questions associated with site-specific geothermal systems, including traditional sandstone/limestone aquifers and repurposed oil/gas reservoirs. Field water was collected from the nearby Tuttle Geothermal Project, which is retrofitting retired oil wells in Tuttle, Oklahoma, to produce geothermal energy for direct heating. Site-specific conditions were used for the experimental setup. We identified the major steel-fluid and reservoir-fluid interactions that may cause potential efficiency degradation of hydrocarbon well converted geothermal systems in operation. By understanding the potential geochemical impacts on geothermal systems, this study provides insights on the geothermal transition from oil/gas fields.

1. INTRODUCTION

Geothermal energy is an energy source that recovers heat from the earth's interior by injecting fluid from the surface through hotter subsurface formations and then extracting the energy from the fluid at the surface. This cycling of the fluid from cold to hot enables the extraction of energy from the subsurface. Geothermal energy has been exploited for decades to generate electricity in both space heating and industrial processes (Barbier, 2002). The present technology makes it possible to control the environmental impact of geothermal exploitation, while remaining economically beneficial (Barbier, 2002).

Studies regarding geothermal systems tend to focus on geothermal, geophysics, geomechanics, and economic benefits (Barbier, 2002; Dickson and Fanelli, 2013; Fridleifsson, 2001; Tester et al., 2006). However, the geochemical impacts of geothermal systems may need more investigation when hydrocarbon wells are used in geothermal applications. During cycling of geothermal fluids above and below surface, the solid-fluid geochemical interactions can cause issues such as pipe corrosion and scaling, affecting recovery efficiency and operation. The geochemical impact of geothermal systems will be site-specific, as the mineralogy and the reservoir fluid chemistry vary with different reservoir sites. Even at the same site, reservoir temperature varies with depth, and temperature has a significant impact on geochemical reactions. Site-specific geochemistry studies for geothermal systems are necessary to provide industrial applicable information.

Many oil and gas reservoirs contain potential geothermal resources. Repurposing depleted hydrocarbon reservoirs and wellbores for geothermal energy recovery is a new concept to increase energy production from existing subsurface infrastructure. Geochemistry has not been studied extensively in such geothermal systems. There are many unknowns to explore regarding the impact of geochemical

reactions on the energy production systems, especially considering that the geochemistry will vary significantly with oil/gas reservoir types, mineralogy, reservoir fluids, etc.

The Oklahoma hydrocarbon field, including the Anadarko basin, has been exploited for over a century to produce oil and gas based on reports from U.S Energy Information Administration (Oh et al., 2023). The Oklahoma Corporation Commission identified that Oklahoma has more than 443,000 oil and gas wells, including plugged, temporarily abandoned, and terminated wells, at a broad range of depths (Oh et al., 2023). The Tuttle Geothermal Project demonstrated the potential of geothermal energy production for direct heat use in two public schools and nearby houses in Tuttle, Oklahoma, via repurposing four existing inactive oil and gas wells (Oh et al., 2023). The target reservoir temperature was estimated to be approximately 90 ℃ at 3 km depth, primarily consisting of Permian to Mississippian Sandstone and Limestone formations (Oh et al., 2023).

The objective of this experimental study is to investigate the geochemical impact of rock-fluid and steel-fluid interactions on the entire geothermal cycling system based on the Tuttle geothermal site conditions. A cycling flow-through system was designed to mimic aboveground steel-fluid interactions and subsurface rock-well-fluid interactions. Field geothermal feed water from the nearby Tuttle Geothermal Project was used as circulating water in the cycling system. Commercial limestone cores and steel cores were cut and fractured for reaction. The results of this study would provide geochemical insights on the use of geothermal energy production in oil/gas fields.

2. MATERIALS AND METHODS

2.1 Experimental Materials

The geothermal feed water was from the field site of the Tuttle Geothermal Project in Tuttle, Oklahoma. After the water was received, it was filtered with a 0.2 μm filtration pump to remove dirt, mud, and microbes for long-term storage. The filtered field water was kept in a refrigerator until it was used for the experiment. Unreacted water was analyzed.

The target reservoir primarily consists of Permian to Mississippian Sandstone and Limestone formations (Oh et al., 2023). For this geochemical experimental study, commercial Lueders Limestone from Kocurek was used as a limestone representative. The Lueders Limestone is predominantly calcite. The elemental composition was analyzed using X-ray fluorescence (XRF, Olympus Vanta VMR) and listed in Table 1.

Table 1: Elemental composition of the Lueders Limestone by XRF.

Element	ppm	Element	ppm
Ca	399,292.6	Cr	19.4
Si	12,458.3	Ni	15.2
Mg	3,522.6	Zn	15.1
Fe	3,000.5	Pb	8.8
Al	2,168.0	Mo	7.4
Ti	513.7	W	5.6
K	397.6	Zr	3.8
Ba	307.3	Hg	3.4
Sr	182.2	Y	2.5
Mn	126.2	Rb	2.2
Cd	21.0	As	0.4

A low-carbon steel rod (8920K231) was purchased from McMaster-Carr. This steel has been used in previous studies as a non-coated experimental representative for oil and gas wellbore materials for corrosion studies during hydraulic fracturing in shale (Mackey et al., 2021; Xiong et al., 2022).

The limestone and steel rods were cut and drilled to 1-inch-diameter, 2-inch-long cores. One limestone core and two steel cores were prepared. The cores were cut into half cylinders and the cut surface was polished with 120 grit sandpaper to remove cutting traces.

2.2 Cycling Experimental System

The experimental system is a cycling system with temperature control (Figure 1). First, the reservoir bottle was filled with 500 mL filtered field water. The water in the bottle was purged with N_2 gas overnight to remove dissolved O_2. Then the N_2 outlet was placed in the headspace to keep N_2 on the headspace to limit direct air contact. However, the system was not in an exact anoxic condition. A sampling tube with a filter at the inlet was placed in the water for liquid sample collection during the experiment.

Polytetrafluoroethylene (PTFE) spacers were used to prop the flow-through channel in the cut cores (Figure 1). The PTFE spacers are 1-mm-thick, 4-mm-wide, and the same length with individual core (2 inch) or stacked cores (4 inch). This was used to create a channel volume of 0.884 cm^3 inside each individual core.

The steel core is individually placed in a rubber sleeve in one core holder at room temperature, which simulated the lowest possible aboveground temperature after geothermal energy was harnessed. The actual returning fluid temperature may be higher than room

temperature. Room temperature was used in the experiment to provide greater difference for comparison with reservoir temperature. The limestone and steel cores were stacked together with limestone encountering the flow first. The stacked core holder was set at 90 ℃. A confining pressure of 300 psi was added on the core holders which hold the cores together. This mimicked the situation when the feed water was injected into the reservoir, heated with geothermal energy, and extracted from the wells. The feed water was pulled from the injection bottle using an injection pump. The water flowed through the individual steel core at room temperature and then into the stacked cores, and finally returned to the injection bottle. As the pressure has less of an impact on chemical reaction rates when compared to temperature in geothermal systems, high-pressure conditions were not considered in this experimental setup.

The flow rate was set at 0.05 mL/min. At this rate, ideally the 500 mL feed water in the bottle would need 7 days to entirely circulate through the system. With the channel volume of 0.884 cm^3, the residence time of the fluid in the three cores would be 53 min. Considering the tubing, the residence time in one cycle would be approximately 1 hour, which is a relevant residence time from a previous report for tracer breakthrough time in geothermal systems (Becker et al., 2013).

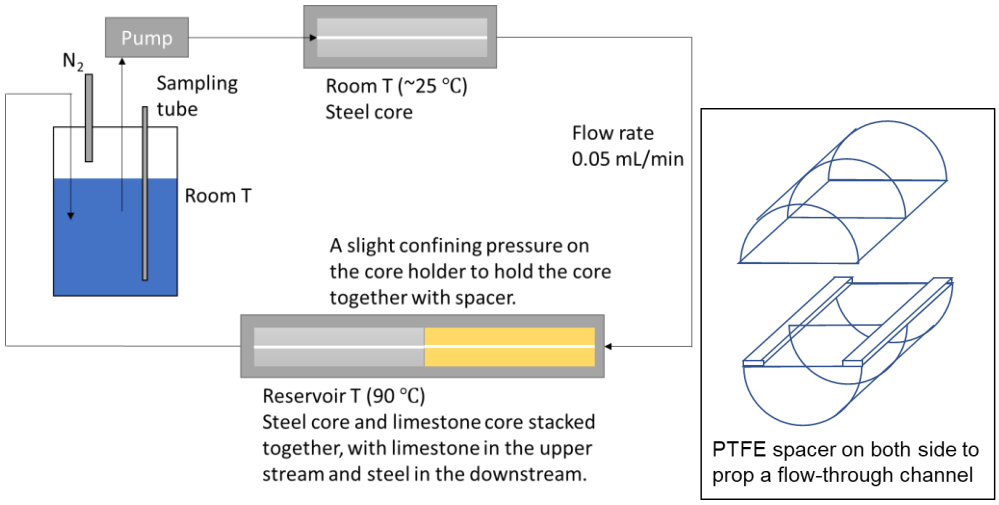

Figure 1: Schematic of experimental cycling system and the stacked core.

Liquid samples were taken intermittently during the reactions. Each liquid sample was less than 7 mL. In total, approximately 30 mL of sample liquid was taken during the experiment. Compared to 500 mL, the water loss would not greatly impact the species concentrations in the feed water bottle. The concentration changes would still reflect the geochemical reactions due to steel/rock/fluid interactions in the cycling system. After 39 days of reaction, the system was shut down and N_2 gas was pumped through the system to push residual fluid into the injection bottle. The final-day sample was taken after the N_2 gas was flushed through the entire system.

2.3 Analysis Methods

The pH of the liquid samples was measured using a handheld pH meter soon after collection. Dissolved total organic carbon (TOC) and non-purgeable organic carbon were analyzed by a TOC analyzer (TOC-L, Shimadzu). Inductively coupled plasma mass spectrometry (ICP-MS, PerkinElmer Nexion 350D), optical emission spectrometry (ICP-OES, Perkin Elmer DV 7300), and ion chromatography (IC, DIONEX ICS-5000, Thermo Scientific) were used to measure the aqueous species concentrations. Mineral saturation indices were calculated using Geochemist's Workbench (GWB) with V8.R6+ database.

The pre-reaction and post-reaction limestone core surface were mapped via digital microscopy (Evident, formerly Olympus) and scanning electron microscope (SEM, Quanta 600F, FEI) with a back-scatter detector (BSE). Point analyses with energy dispersive spectroscopy (EDS, Oxford) were performed with SEM. The limestone core was scanned using X-ray computed tomography (CT, M5000 Industrial Computed Tomography System, North Star Imaging) with the core inside the sleeve at ambient conditions before and after the reaction. CT images were processed using ImageJ (Rasband, 1997).

Steel analysis was performed by taking 3D images of the steel surface in an electron microscope (Evident, formerly Olympus). The data was then extracted. Root mean square (RMS) roughness and average roughness (Ra) metrics were determined in Python 3.9 using the Pandas and Numpy packages. Unreacted steel surface roughness data was used as baseline correction.

3. RESULTS AND DISCUSSION

3.1 Fluid Sample Analysis

3.1.1 Reservoir Fluid Photos

The color of reservoir fluid noticeably changed during the reaction (Figure 2). Before the reaction, the fluid was clear. Within a few days of the reaction, the fluid turned orange due to mineral precipitates that were brought back from the cycling pathway. As the reaction continued, obvious orange flecks were observed in the reservoir fluid. Purple/red precipitates coated the inside of the returning

tube to the reservoir bottle (Figure 2). The tube was transparent before the reaction. These precipitates were identified as iron oxides via SEM.

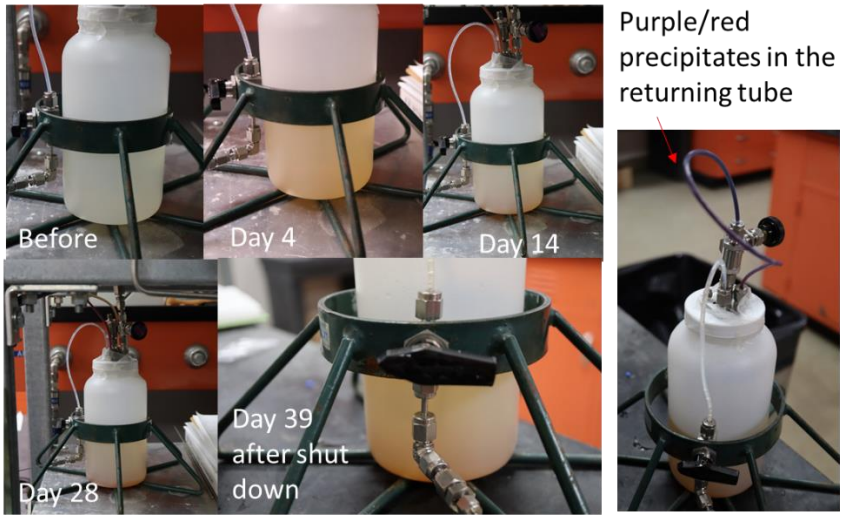

Figure 2: Reservoir bottle photos during reaction.

3.1.2 Fluid Chemistry

Initially, the feed water was slightly acidic. The fluid pH decreased from 6.6 to 5.4 within approximately 10 days of reaction (Figure 3).

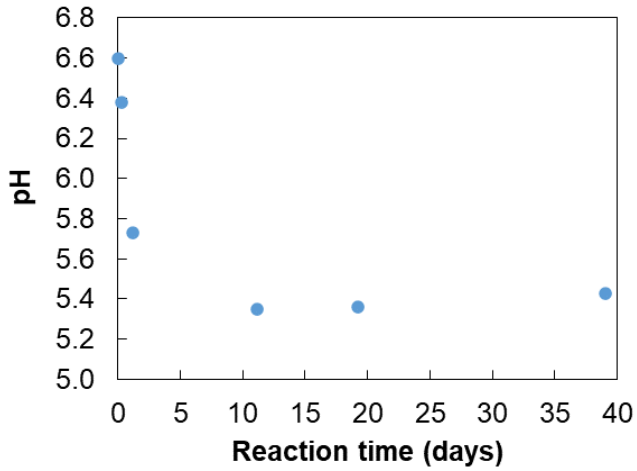

Figure 3: pH changes of the liquid samples with reaction time.

Figure 4 shows how the aqueous species concentrations change with reaction. The data point at Day 0 represents the pre-reaction reservoir fluid. The last sample was taken after using N_2 gas to purge the residual fluids in the tubing and fractured cores back to the reservoir bottle. Cations like Fe, Zn, Cr, Ni, and Cu (and trace Co, Mo, Pb) shared a similar trend. The concentration increased over 20 days of reaction, and in the last sample the concentration decreased significantly. During the reaction, they were most likely released from the steel core. The release of Fe^{2+} into liquid was the first step for iron corrosion. Although N_2 gas was in the reservoir bottle headspace, the system was not in a strictly anoxic environment. There was still dissolved O_2 to oxidize aqueous Fe^{2+} that formed iron oxides precipitates. The drastic concentration decrease in the last sample may be because the local chemistry in the core fractures and tubing were different with the bulk reservoir fluid chemistry. By flushing the residual fluid from these zones to the bulk reservoir fluid, the chemical equilibrium regarding these cations were broken and new precipitation reactions associated with these cations were triggered.

Aqueous silica decreased to an undetectable concentration, indicating silicate mineral formation in the system. Major cations such as Ca, Mg, Na, and Sr and major anions such as Cl, Br, and sulfate did not show significant changes throughout the reaction.

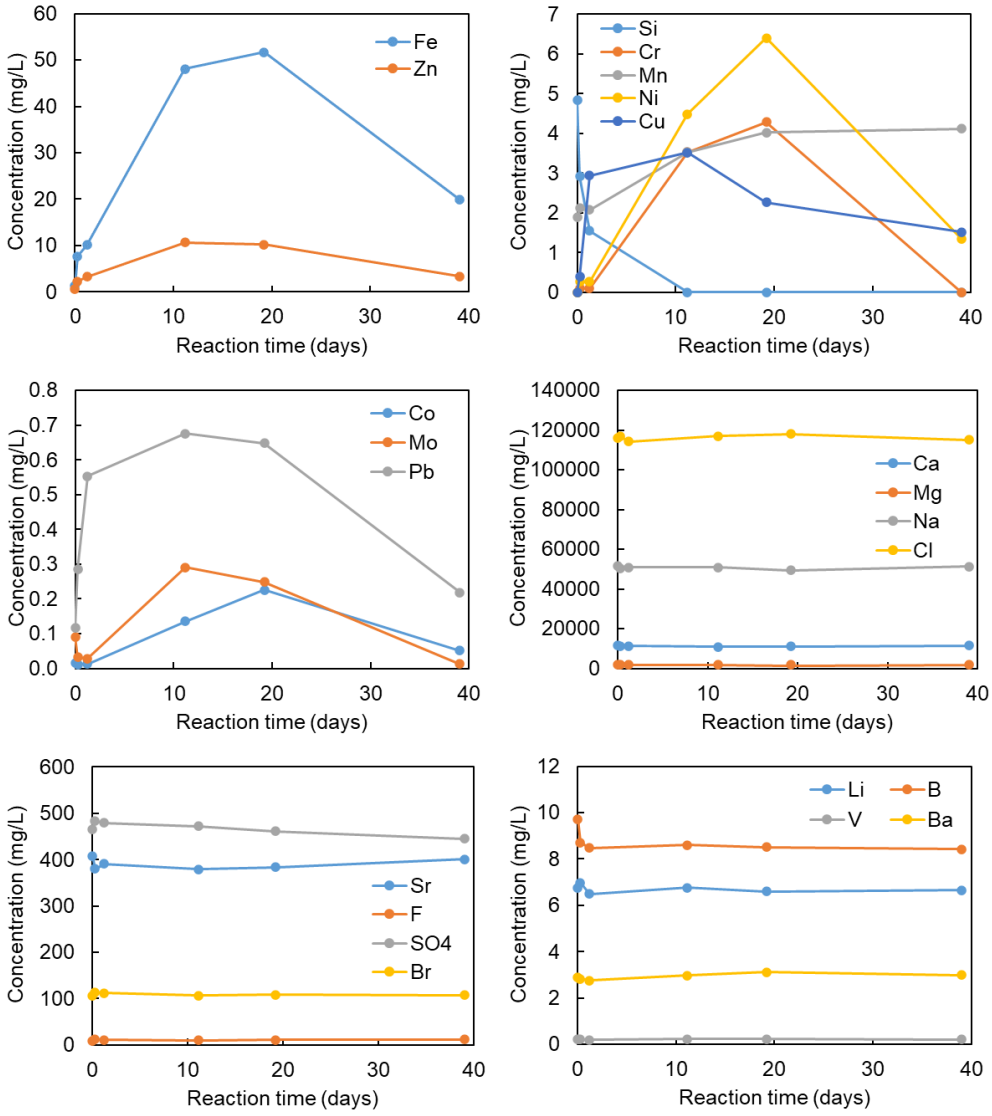

Figure 4: Species concentrations of the liquid samples with reaction time.

The dissolved inorganic carbon (DIC) in the pre-reaction reservoir fluid was minimal (3.4 mg/L), and decreased to barely detectable after the reaction (Table 2). With the stable Ca concentration throughout the reaction in Figure 4, the limestone-fluid interactions did not seem to dissolve calcite to release Ca or carbonate into the fluid. The non-purgeable organic carbon increased after the reaction. This may be due to small residual organic matter in limestone or deterioration of the PTFE spacers at high-temperature and high-pressure environments.

Table 2: DIC and non-purgeable organic carbon (NPOC) concentrations before and after reaction in the reservoir bottle.

	DIC (mg/L)	NPOC (mg/L)
Pre-reaction	3.4	96.9
Post-reaction	0.8	245.7

3.1.3 Saturation Index Calculation

Mineral saturation indices were calculated based on the water chemistry (Table 3). Multiple secondary minerals were predicted to precipitate, such as phosphates, chromites, and iron oxides.

Table 3: Mineral saturation indices (log Q/K) calculated based on aqueous species concentrations.

Days/Minerals	Pre-Reaction	0.3	1.2	11.2	19.2	39 (Post-Reaction)
Fluorapatite		16.63				
$ZnCr_2O_4$		16.62	13.29	12.96	13.03	
Chromite		11.99	8.58	8.434	8.573	
$CuFeO_2$		10.43	8.836	8.051	7.921	7.642
$CuCr_2O_4$		9.271	6.614	5.867	5.782	
Magnesiochromite		8.369	4.842	4.019	4.123	
Hydroxylapatite		4.603				
Karelianite	4.16	3.721	2.294	1.614	1.651	1.742
Pyromorphite		2.637				
$MnHPO_4$		1.617				
Fluorite	1.374	1.615	1.539	1.444	1.536	1.617
Whitlockite		1.458				
Barite	0.6717	0.6886	0.6682	0.7016	0.7152	0.669
$PbHPO_4$		0.476				
Sellaite	0.2015	0.4483	0.3718	0.2881	0.3659	0.449
Quartz	0.2546	0.03947	-0.2295			
Tridymite	0.08314	-0.132	-0.401			

3.2 Limestone Characterization

3.2.1 SEM Analysis

The pre-reaction limestone core is primarily composed of calcite, with a small amount of barite, phosphate, and silicates (Figure 5). The SEM-EDS analysis is consistent with the XRF analysis.

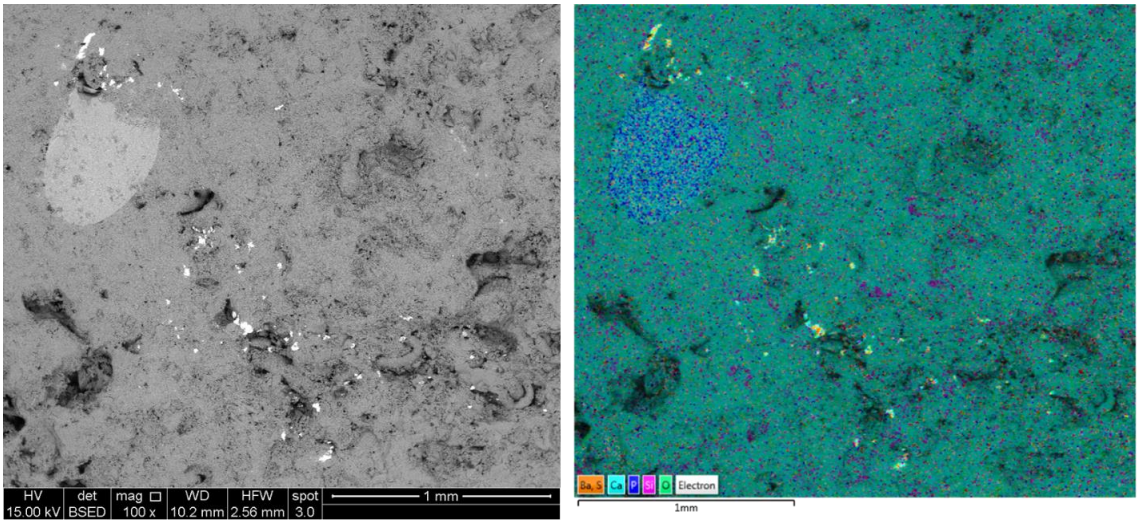

Figure 5: SEM-EDS map analysis on a selected area of pre-reaction limestone surface.

The reacted surface of the limestone core was mapped using SEM and an electron microscope (Figure 6). Most of the secondary precipitates found are sodium chloride, salts from residual water evaporation, even though N_2 gas was flushed through the system after the reaction. The four corners marked by the red boxes in Figure 6 were rich in carbon and were found using SEM-EDS, which may be due to the PTFE spacers.

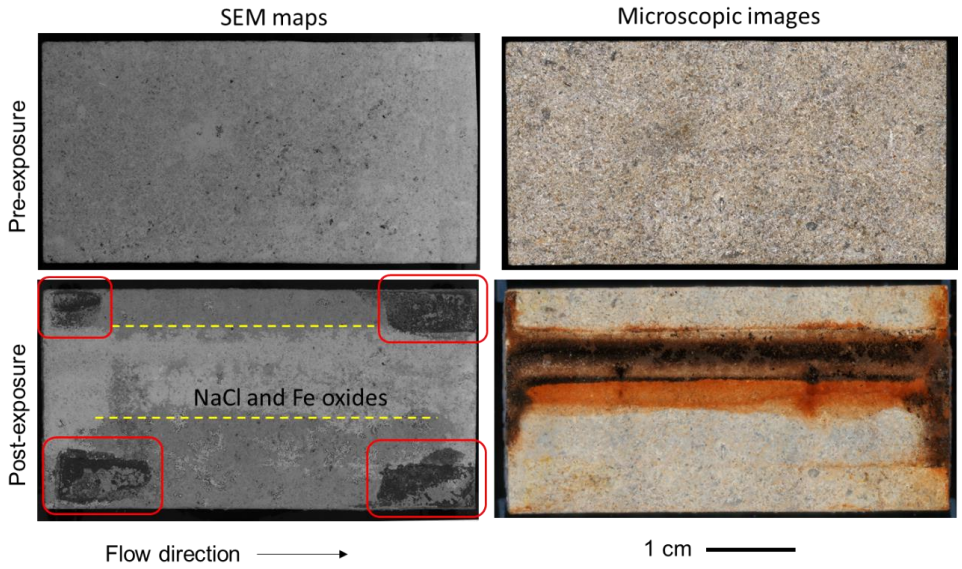

Figure 6: SEM maps and microscopic images of one core surface before and after reaction. Precipitates in the channels are predominantly salt from residual water, and some Fe oxides from steel/fluid reactions. Red box areas are rich in carbon in EDS which may be residuals from the PTFE spacers.

Iron oxides were observed as brighter precipitates than sodium chloride in SEM-EDS. Iron oxides are covered or mixed in the residual salts, which formed post-reaction. The Fe for iron oxide precipitation was primarily from Fe corrosion in the precedent fluid-steel interaction at ambient condition.

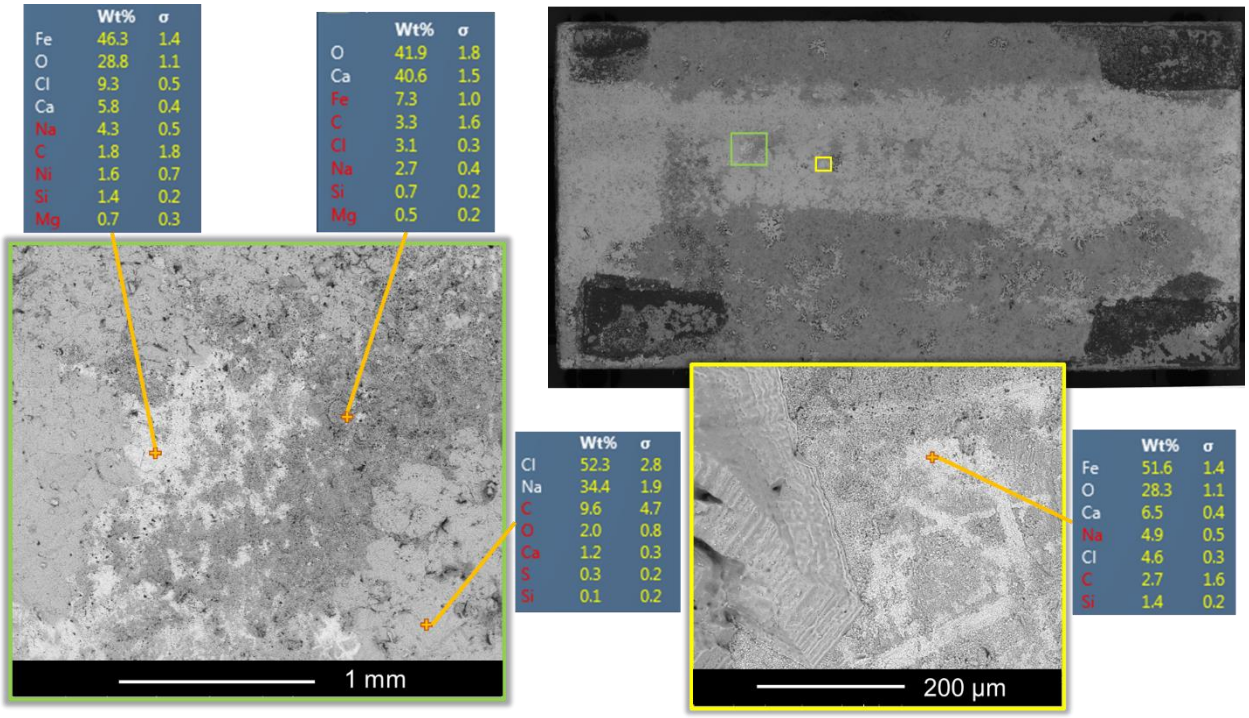

Figure 7: SEM-EDS spot analysis on selected areas of reacted limestone core surface.

3.2.2 X-Ray CT Scan

CT images on the reacted surface did not show obvious pore volume change due to the resolution limit (Figure 8). Half of the limestone core was broken in the core holder, which may be a result of the confining pressure, pressurization/depressurization of the experiment, and extraction of the sample from the core holder to CT scan.

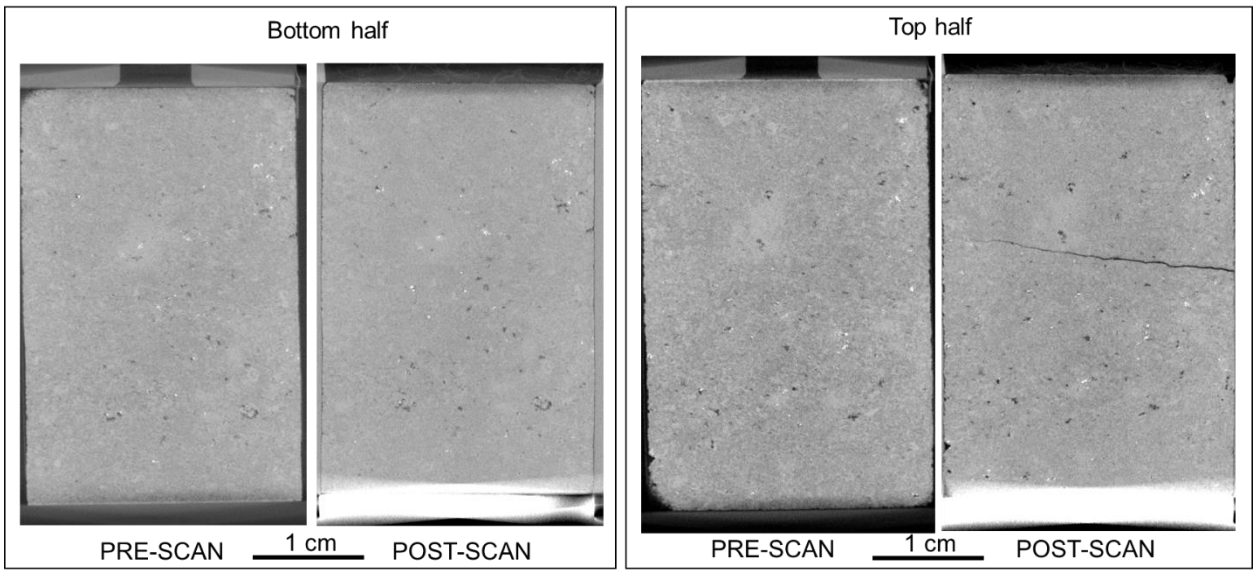

Figure 8: Pre-reaction and post-reaction limestone core CT image. Flow direction is from bottom to top. The bright region at the bottom of the post-reaction scan is due to stacked steel core interference in CT.

3.3 Steel Corrosion Analysis

3.3.1 Surface Mapping

The unreacted steel core surface was barely oxidized. Post reaction steel cores were corroded to a different extent. The microscopic images of the steel surface after the reaction showed that the individual steel core was less corroded than the stacked steel core. The surface of the stacked steel core at elevated temperatures was almost entirely covered with orange/red rust.

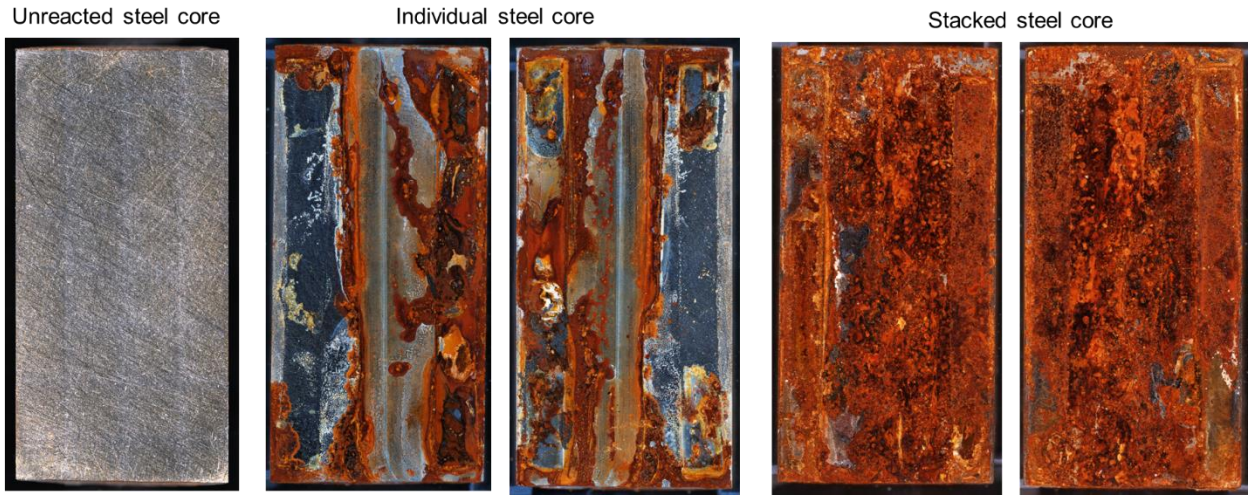

Figure 9: Microscopic images of the surface of unreacted steel core, post-reaction stacked steel core, and post-reaction individual steel core. Flow direction is from bottom to top.

3.3.2 Roughness Analysis

Surface roughness analysis is a widely used application to measure the variation surface topography of materials (Durakbasa et al., 2011; Lee and Cho, 2012), and can be used as a metric for evaluating the severity of impacts to tubing exposed to produced fluids in subsurface applications. Profilometers are typically used to take a direct mechanical measurement of deviations in heights by dragging a stylus across the sample surface; however, this method can be destructive to minerals formed on the sample surface, such as corrosion products, during the measurement.

To prevent surface alterations of the sample, surface roughness measurements were taken using variable focus microscopy. Images and measurements were taken at the red spots shown in Figure 10 at the inflow, center, and outflow core positions of the stacked steel core sections. The spots parallel to the flow direction within the flow conduit are shown in Figure 11 and spots under the spacers in Figure

12. Next, the surface roughness profiles were plotted (Figure 11, 12) and used to calculate RMS and Ra metrics in Python 3.9 using the Pandas and Numpy packages. Then, surface roughness analysis was done on an unreacted surface for a baseline comparison.

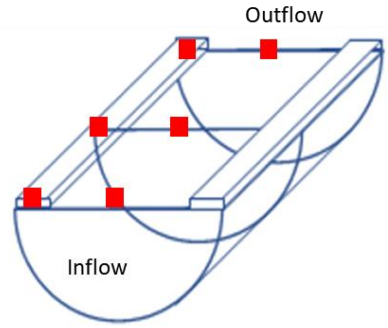

Figure 10: Locations of imaging and analysis conducted on a reacted sample surface using an Olympus DSX100 Digital microscope.

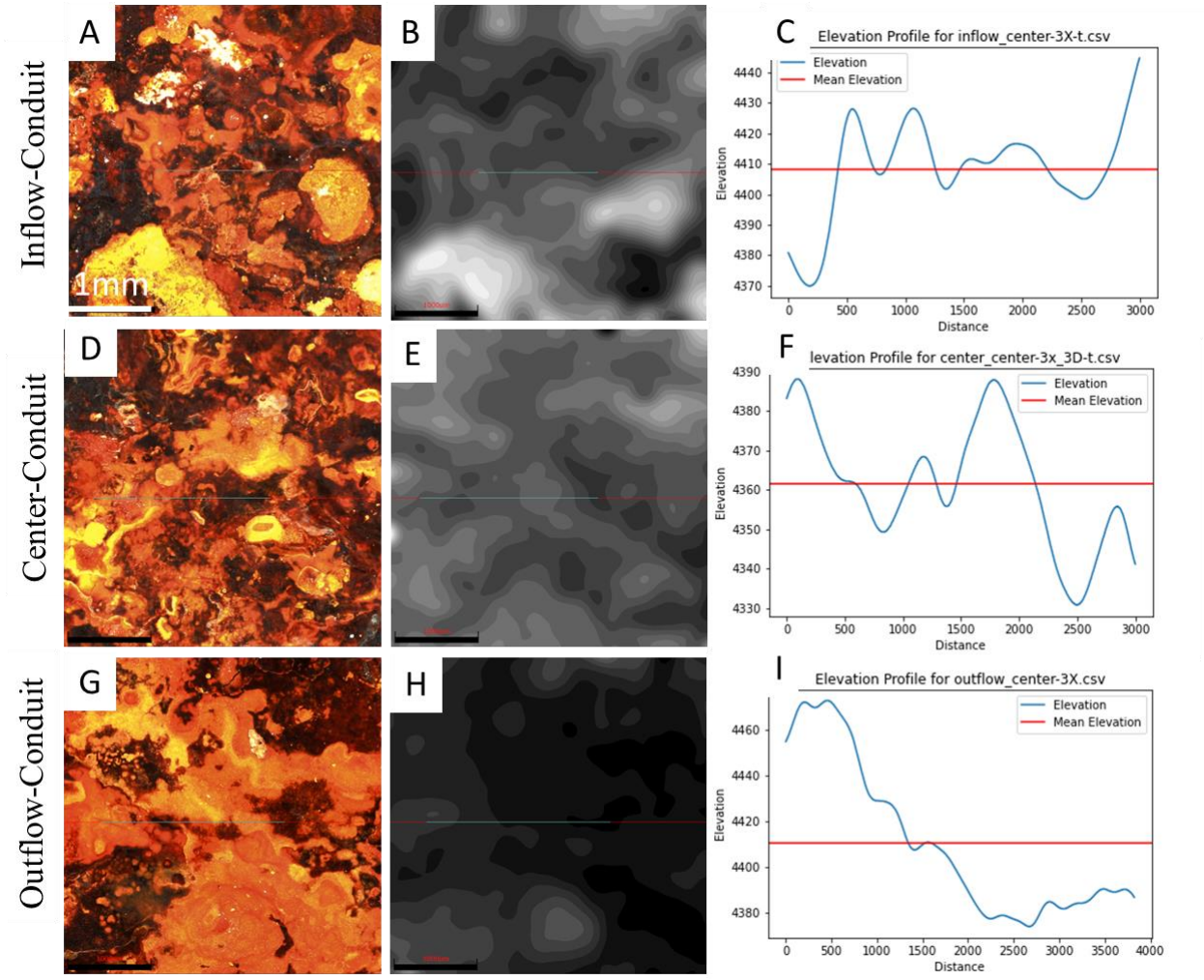

Figure 11: True color photomicrographs (A, D, G) and elevation maps (B, E, H) taken at the inflow, center, and outflow positions within the flow conduit. Images were taken at 3x magnification. Surface roughness profiles (C, F, I) were plotted parallel to the direction of flow. Distance unit in the x-axis is micrometers.

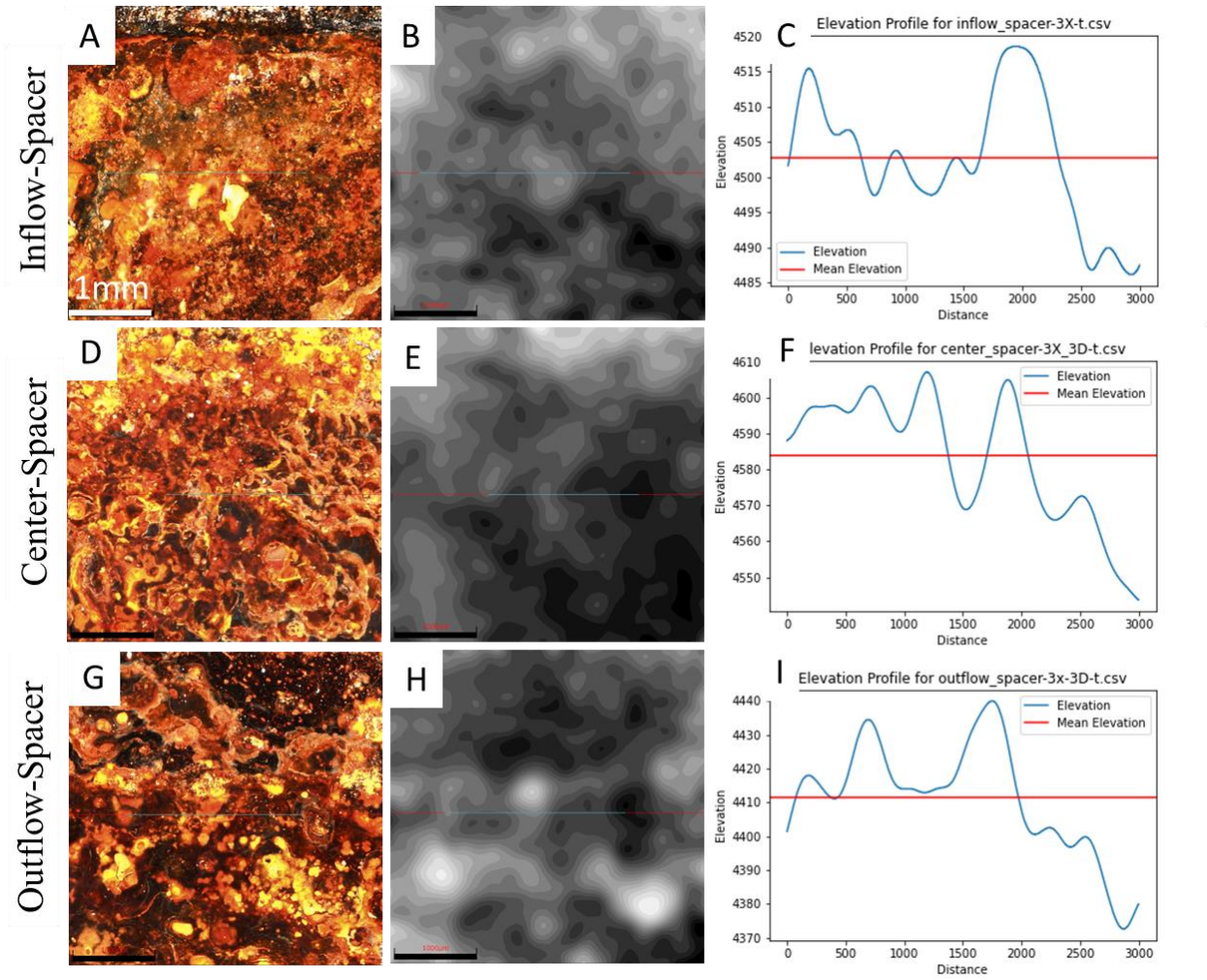

Figure 12: True color photomicrographs (A, D, G) and elevation maps (B, E, H) taken from the spacer area at the inflow, center, and outflow sample positions. Images were taken 3x magnification. Surface roughness profiles (C, F, I) were plotted parallel to the direction of flow. Distance unit in the x-axis is micrometers.

Results show that corrosion induced surface roughness increased in both the conduit and spacer locations during flow compared to the unreacted steel sample, though the magnitude varied by location along the flow path (Table 4). The inflow and center conduit Ra and RMS roughness calculations were similar with ranges of 12.8-15.2 µm and 15.3-16.5µm, respectively. The outflow conduit location had the largest increase in Ra (30.5 µm) and RMS (34.8 µm). Spacer Ra and RMS roughness values were lowest at the inflow location (7.4 and 9.3 µm) compared to the center and outflow locations. The increases in surface roughness at each sample location were small and would likely not result in serious impacts to fluid flow over the time span observed in this study.

Table 4. RMS and Ra measurements taken at various locations on the reacted steel sample. Surface roughness profiles were taken from the conduit and spacer regions at inflow, center, and outflow points.

Measurement Location	RMS (µm)	Ra (µm)
inflow-conduit	15.3	11.1
inflow-spacer	9.3	7.4
center-conduit	15.6	12.6
center-spacer	17.2	15.2
outflow-conduit	34.8	30.5
outflow-spacer	16.5	12.8
unreacted sample	0.7	0.6

3.4 Geochemical Impact Along the Geothermal Cycling Pathway

From the liquid and solid analysis, steel-fluid reactions had greater impact on the entire cycling system than rock-fluid reactions. Limestone dissolution occurred, but was limited compared to Fe released from the steel. There were limited secondary precipitates due to limestone-fluid interactions. The salts from water evaporation may be a scale mineral during geothermal cycles at different temperatures. Although aqueous silica was released from the rock, no obvious silicate scale minerals were observed. The small amount of secondary minerals resulting from limestone-fluid reactions was not a concern for fluid transport.

Steel corrosion was obvious in both aboveground and reservoir temperature samples. The increase in temperature accelerates electrochemical, chemical reactions, mass transfer, diffusion of corrosive species to the surface, etc., involved in the corrosion process (Kahyarian and Nesic, 2020; Nešić, 2007). This explains why the stacked steel core at 90 ℃ showed significantly more rust covering the reaction surface than the steel at room temperature. In real geothermal operations, the geothermal output temperature associated with aboveground steel materials can be much higher than room temperature. Room temperature was selected in the experiment to show the corrosion difference at the least optimal condition.

The migration of iron oxides from steel corrosion along the cycling pathway may be a potential issue for the geothermal system. The cycling fluid could carry dissolved species and scale minerals to the entire geothermal circulating system. The orange rust was found in the tubing, the reservoir rock, and the injection bottle. The corrosion rust increased the roughness of steel surface but the main flow channel was not blocked. However, these scale minerals could form deposits on heat exchanger surfaces, reducing heat transfer efficiency, increasing energy consumption, and may lead to mechanical damage in the long term (Penot et al., 2023).

4. CONCLUSION

The impact of geochemicals on geothermal systems should consider the entire fluid cycling pathway. Dissolved species and scaling minerals can be carried with the fluid away from its origin and may cause issues at other locations. The salt scale minerals from the evaporation of fluid may be a concern with temperature shifts in different parts of the cycle. Temperature has a major impact on iron corrosion in geothermal systems. Iron oxides from steel corrosion was observed prevalently along the cycling pathway. Prevention and control of steel corrosion is necessary for geothermal systems.

ACKNOWLEDGEMENTS

This work was performed in support of the U.S. Department of Energy's (DOE) Laboratory Directed Research & Development (LDRD) program and executed through the National Energy Technology Laboratory (NETL) Research & Innovation Center consistent with the authorizing legislation and DOE LDRD Order 413.2C. Thanks to the people who assisted the X-ray CT scan and technical team at NETL Morgantown and the analysts at NETL Pittsburgh Analytical Laboratory.

DISCLAIMER

This project was funded by the United States Department of Energy, National Energy Technology Laboratory, in part, through a site support contract. Neither the United States Government nor any agency thereof, nor any of their employees, nor the support contractor, nor any of their employees, makes any warranty, express or implied, or assumes any legal liability or responsibility for the accuracy, completeness, or usefulness of any information, apparatus, product, or process disclosed, or represents that its use would not infringe privately owned rights. Reference herein to any specific commercial product, process, or service by trade name, trademark, manufacturer, or otherwise does not necessarily constitute or imply its endorsement, recommendation, or favoring by the United States Government or any agency thereof. The views and opinions of authors expressed herein do not necessarily state or reflect those of the United States Government or any agency thereof.

REFERENCES

Barbier, E., 2002. Geothermal energy technology and current status: an overview. Renewable and sustainable energy reviews 6, 3-65.

Becker, M.W., Remmen, K., Reimus, P.W., Tsoflias, G.P., 2013. Investigating well connectivity using ionic tracers, Thirty-Eighth Workshop on Geothermal Reservoir Engineering, Stanford, California.

Dickson, M.H., Fanelli, M., 2013. Geothermal energy: utilization and technology. Routledge.

Durakbasa, M.N., Osanna, P.H., Demircioglu, P., 2011. The factors affecting surface roughness measurements of the machined flat and spherical surface structures–The geometry and the precision of the surface. Measurement 44, 1986-1999.

Fridleifsson, I.B., 2001. Geothermal energy for the benefit of the people. Renewable and sustainable energy reviews 5, 299-312.

Kahyarian, A., Nesic, S., 2020. On the mechanism of carbon dioxide corrosion of mild steel: Experimental investigation and mathematical modeling at elevated pressures and non-ideal solutions. Corrosion science 173, 108719.

Lee, D.-H., Cho, N.-G., 2012. Assessment of surface profile data acquired by a stylus profilometer. Measurement science and technology 23, 105601.

Mackey, J., Gardiner, J., Kutchko, B., Brandi, M., Fazio, J., Hakala, J.A., 2021. Characterizing mineralization on low carbon steel exposed to aerated and degassed synthetic hydraulic fracture fluids. Journal of Petroleum Science and Engineering 202, 108514.

Nešić, S., 2007. Key issues related to modelling of internal corrosion of oil and gas pipelines–A review. Corrosion science 49, 4308-4338.

Oh, H., Akar, S., Davalos Elizondo, E., Vivas, C., Salehi, S., 2023. Subsurface Characterization for Evaluating Geothermal Resource Potential from Existing Oil and Gas Wells in Tuttle, Oklahoma. National Renewable Energy Laboratory (NREL), Golden, CO (United States).

Penot, C., Martelo, D., Paul, S., 2023. Corrosion and scaling in geothermal heat exchangers. Applied Sciences 13, 11549.

Rasband, W., 1997. ImageJ. US National Institutes of Health, Bethesda, MD, USA.

Tester, J.W., Anderson, B.J., Batchelor, A., Blackwell, D., DiPippo, R., Drake, E., Garnish, J., Livesay, B., Moore, M., Nichols, K., 2006. The future of geothermal energy. Massachusetts Institute of Technology 358.

Xiong, W., McAdams, B., Stuckman, M., Kutchko, B., Lopano, C., Hakala, J.A., 2022. The Impact of Hydraulic Fracturing Fluid on the Near-Wellbore Shale Region Involving Interactions with Steel, Cement and Shale, Proceedings of the 10th Unconventional Resources Technology Conference.